Journal of Agricultural Engineering

https://www.agroengineering.org/

Structural design, modeling and simulation analysis of a cage broiler inspection robot

Yongmin Guo,[1,2*] Xinwei Yu,[2*] Wanchao Zhang,[1,2] Changxi Chen,[1,2] Liji Yu[2]

[1]Key Laboratory of Smart Breeding, Ministry of Agriculture and Rural Affairs, Xiqinq District, Tianjin
[2]School of Computer and Information Engineering, Tianjin Agricultural University, Xiqinq District, Tianjin, China

*these authors share first authorship.

Corresponding author: Wanchao Zhang, Key Laboratory of Smart Breeding, Ministry of Agriculture and Rural Affairs, 22 Jin jing Road, Xiqinq District, 300384 Tianjin, China.
E-mail: 821392902@qq.com

Publisher's Disclaimer

E-publishing ahead of print is increasingly important for the rapid dissemination of science. The *Early Access* service lets users access peer-reviewed articles well before print/regular issue publication, significantly reducing the time it takes for critical findings to reach the research community.

These articles are searchable and citable by their DOI (Digital Object Identifier).

Our Journal is, therefore, e-publishing PDF files of an early version of manuscripts that undergone a regular peer review and have been accepted for publication, but have not been through the typesetting, pagination and proofreading processes, which may lead to differences between this version and the final one.

The final version of the manuscript will then appear on a regular issue of the journal.

Please cite this article as doi: 10.4081/jae.2025.1806

©The Author(s), 2025
Licensee PAGEPress, Italy

Submitted: 5 April 2024
Accepted: 25 March 2025

***Note**: The publisher is not responsible for the content or functionality of any supporting information supplied by the authors. Any queries should be directed to the corresponding author for the article.*

All claims expressed in this article are solely those of the authors and do not necessarily represent those of their affiliated organizations, or those of the publisher, the editors and the reviewers. Any product that may be evaluated in this article or claim that may be made by its manufacturer is not guaranteed or endorsed by the publisher.

Structural design, modeling and simulation analysis of a cage broiler inspection robot

Yongmin Guo,[1,2*] Xinwei Yu,[2*] Wanchao Zhang,[1,2] Changxi Chen,[1,2] Liji Yu[2]

[1]Key Laboratory of Smart Breeding, Ministry of Agriculture and Rural Affairs, Xiqinq District, Tianjin
[2]School of Computer and Information Engineering, Tianjin Agricultural University, Xiqinq District, Tianjin, China

*these authors share first authorship.

Corresponding author: Wanchao Zhang, Key Laboratory of Smart Breeding, Ministry of Agriculture and Rural Affairs, 22 Jin jing Road, Xiqinq District, 300384 Tianjin, China. E-mail: 821392902@qq.com

Abstract
When designing an inspection robot for cage-reared broiler chickens, it is imperative to meticulously contemplate both the performance of the robot within the designated workspace and its energy efficiency. The paper optimizes the structure and energy consumption of the robot by analyzing its working environment and the power usage associated with its lifting and lowering functions. Inspection robots designed for cage-reared broiler chickens are required to operate within densely populated chicken coops, underscoring the critical importance of the structure and maneuverability these machines. This research utilizes a four-wheel skid-steering drive mechanism to facilitate swift and precise turns, empowering the robot to adeptly navigate the confined spaces within the chicken coops. The mathematical description of the robot is based on a static kinematic model to ensure efficient navigation within the enclosed environment. The mechanical framework of the robot comprises a four-wheel drive system crafted from hollow rectangular low-carbon steel bars. This design provides the necessary strength and durability while maintaining a lightweight profile. Additionally, the incorporation of a five-axis mechanical arm, integrated with sensors and a gimbal lifting algorithm, ensures adaptability to intricate inspection spaces, with a focus on energy efficiency. Simulation analysis based on the developed model demonstrates the suitability of this structure for the application of inspection robot for cage-reared broiler chickens, ensuring stable operation within the chicken coops. Furthermore, in an effort to boost the energy efficiency of the robot, an analysis of the power consumption linked to its lifting and lowering functions is undertaken. By integrating energy-efficient design principles and intelligent control strategies, the lifting and lowering functions of the system can reduce energy consumption.

This ensures the completion of tasks, prolongs battery life, and ultimately enhances the work efficiency and sustainability of the robot.

Key words: broiler; dynamics analysis; inspection robot; kinematics analysis.

Introduction

In the poultry industry, the challenges posed by confined spaces have been a persistent concern (Xie *et al*., 2022). These environments often restrict the smooth execution of tasks such as maintenance, equipment monitoring, and coop cleaning (Nguyen *et al*., 2020). They are characterized by limited space and high stacking density, leading to poor air circulation. This results in insufficient oxygen supply and an increase in the concentration of harmful gases, including ammonia (NH_3), hydrogen sulfide (H_2S), and carbon monoxide (CO) (Xiao *et al*., 2019). Furthermore, the proximity of personnel to mechanical equipment and electrical systems increases potential risks (Rea and Ottaviano, 2018). To address these challenges, researchers have explored the application of robot systems in similar confined space environments (Ren *et al*., 2020). This includes the use of mobile robots equipped with integrated electronic noses (e-noses) for monitoring hazardous substances (Sun *et al*., 2019). These robots employ a four-wheel skid-steering drive mechanism to ensure precise operation within tight spaces (Tzitzis *et al*., 2019). Additionally, they utilize a static kinematic model to ensure structural stability when dealing with hazardous substances (Cheng and Xiang, 2020). The extensive use of robots in various industrial applications has also provided valuable insights into addressing confined space issues. Engineers have employed tools like SolidWorks simulation and Robot Analyzer for the design (Karpyshev *et al*., 2021), simulation, and analysis of six-axis robots, catering to industrial requirements. These studies emphasize the significance of maintaining chassis stability during robot motion and ensuring that robotic arms offer flexibility and precision (Cai *et al*., 2021).

The case of food delivery robots with suspension-damping structures underscores the crucial role such structures play in tackling complex terrains and environments (Razak *et al*., 2016). Through dynamic analysis and simulations (Yang *et al*., 2021), researchers have verified the rationality and stability of the design using tools like Adams, ensuring reliable operation under rugged conditions.

Collectively, these research findings offer essential insights and solutions for addressing confined space challenges in the poultry industry. This paper optimizes the structure and energy consumption of the robot by analyzing its operating environment and power consumption related to the lifting function. A four-wheel skid-steering drive mechanism is employed for rapid and precise turns, allowing the robot to adapt to confined coop spaces. The mathematical description of the robot relies on a static kinematic model to ensure effective navigation in a confined environment. The mechanical structure of the robot includes a four-wheel drive system constructed using hollow rectangular mild steel bars, offering the required strength and durability while maintaining a lightweight design. Additionally, a five-axis robotic arm with sensors and universal joint lifting algorithms ensures adaptability to complex inspection spaces while prioritizing energy efficiency.

Materials and Methods

The chassis and robotic arm gimbal are critical components of the cage-reared broiler inspection robot system (Quaglia *et al*., 2019). The performance of these two components directly affects the inspection efficiency and power consumption of the inspection robot (Paradkar *et al*., 2021). A robotic arm gimbal with acceptable performance can achieve high-level maneuverability at the inspection position and adapt to complex inspection environments and broiler postures (Raikwar *et al*., 2022). Different inspection motion strategies can also affect the power consumption of the robotic arm under the same inspection trajectory (Zhao *et al*., 2019). Therefore, the evaluation of the cage-reared broiler inspection robot needs to be analyzed from the two aspects of inspection ability and power consumption.

Design and working principle of the caged chicken inspection robot chassis and manipulator turret

The inspection robot for caged chickens is specifically designed to navigate through the chicken coop and assess the health and well-being of the chickens (Yoo and Huh, 2020).

The robot comprises a mobile chassis and a manipulator turret, as depicted in Figure 1a. It consists of a motion chassis and a sensor gimbal, weighing approximately 80 kg. When contracted, the robot measures 400 mm × 500 mm × 700 mm (height × length × width). The chassis is strategically designed to cover the entire working area of the chicken house (Xue *et al*., 2023), while the gimbal has a working range of 1500 mm × 200 mm (height × width). The chassis of the robot, as shown in Figure 1 a-1, is equipped with a four-wheel differential drive system to achieve agile movement and stability. Wheel encoders are used for odometry-based localization. For autonomous navigation within the coop, a magnetic tape is employed for coarse navigation, while RFID tags are utilized for precise localization (Mishra *et al*., 2019). The chassis also features a Pan-tilt turret, which mounts a 5-DOF "P-R-RP-R-R" type manipulator. This manipulator includes a camera, temperature sensor, CO_2 sensor, wind sensor, and humidity sensor to inspect chicken health.

Furthermore, the robotic arm gimbal (Figure 1 a-3) consists of five rotational joints, which are driven by step motors through a worm gear mechanism. This design allows for narrow passage navigation and provides a vertical working range of 1500 mm in height and 200 mm of forward reach.

The mobility choice for this robot is a four-wheel configuration due to its superior stability, load capacity, simple control, and excellent maneuverability, as confirmed by research (Yoo *et al*., 2020; Xu *et al*., 2021; Saeedi *et al*., 2021). Additionally, the model was created in

SolidWorks, constructed from aluminum, and defined with connection relationships and motion constraints for dynamic model parameter acquisition.

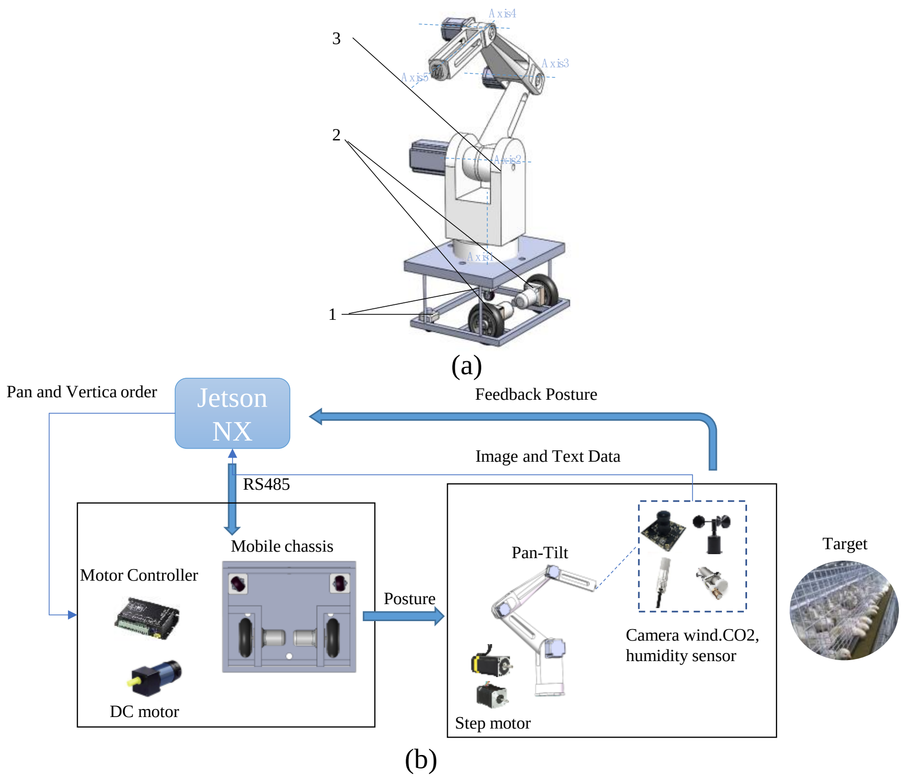

Figure 1. Mechanical and control structure of caged chicken inspection robot. a) Model design of the caged chicken inspection robotic mobile chassis and Sensor-Pan-tilt, and internal structure design of the caged chicken inspection robotic mobile chassis and Sensor-Pan-tilt. 1. Two parallel mounted universal wheels; 2. two parallel mounted drive wheels; 3. sensor Pan-Tilt for spatial motion. b) Schematic diagram of inspection robot control.

Analysis of the motion performance of a mechanical arm

Parameter solution of robotic arm based on Newton polynomial

The sensor gimbal is responsible for the vertical movement of the sensors that collect environmental and chicken data in the chicken house (Zhang *et al*., 2022). The following characteristics should be primarily considered: 1) sufficient vertical and forward work range to enable the inspection robot to have adequate working height and forward distance, and 2) the overall stability of the robot should be maintained in the extended and raised state (Zhang and Han, 2020).

We chose a five-axis robotic arm mainly for the following reasons:

1) The activity space in the chicken house is limited, requiring the robotic arm to be able to retract into a compact posture to pass through narrow spaces.

2) Flexible adjustment: due to the influence of different chicken house environments (such as varying cage heights and obstructions), different ages of the chickens, and different

shooting distances, it is necessary to adjust the position and orientation of the camera in real-time to obtain clear and consistent images, the Pan-tilt 3-D SW model, as shown in Figure 2. The sensor gimbal consists of five links with five degrees of freedom, and the main controlled joints are the second, third, and fourth joints. The sensor support bracket is mounted on the fifth joint that carries the sensor gimbal. During inspection, the stepper motor of the fifth joint maintains a fixed angle, and then when the robot starts inspection and detects that it is at the initial position, the second, third, and fourth joints move downward in linkage to the first layer. After the chassis completes the first-layer inspection of the entire chicken house along the track, the sensor is raised and extended to the second layer of the chicken cage by the second, third, and fourth joints, which may not be at the same depth as the first layer. The extension ensures that the sensor bracket is closer to the chickens.

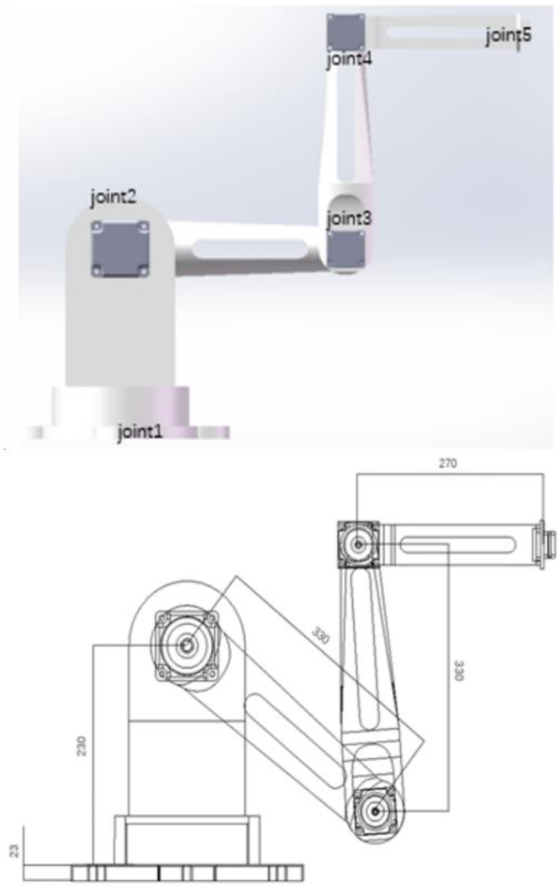

Figure 2. Pan-Tilt 3-D SW model.

All the links of the Pan-Tilt are connected in series alternately, starting with the bottom link and ending with the end link. Catanoso *et al*. (2021) investigated the impact of different materials on the performance of the Pan-Tilt. All the connecting rods of the Pan-Tilt are made of aluminum (Chen *et al*., 2021). We chose aluminum as the connecting rod material because of its light weight, corrosion resistance and good cutting performance. Aluminum is one-third as dense as steel and has good strength in low-weight structures. It is easy to work with processes such as milling, drilling, cutting and stamping (Almasri *et al*., 2021). In addition, the energy required for processing operations is very low (Liu *et al*., 2022). Aluminum is very resistant to corrosion in humid environments. The detailed information of connecting rod length is shown in Table 1. Each joint has a specific range of rotation, as shown in Table 2. DH (Le *et al*., 2019) constraints are obtained by solving the forward kinematics, as shown in Table 3. Where, coordinate system i is defined as ${}_{i=1}^{\;i}\mathbf{A}$, as shown in Eq. l:

$${}_{i=1}^{\;i}\mathbf{A} = \begin{bmatrix} \cos\theta_i & -\sin\theta_i\cos\alpha_i & \sin\theta_i\sin\alpha_i & \alpha_i\cos\theta_i \\ \sin\theta_i & \cos\theta_i\cos\alpha_i & -\cos\theta_i\sin\alpha_i & \alpha_i\sin\theta_i \\ 0 & \sin\alpha_i & \cos\alpha_i & d_i \\ 0 & 0 & 0 & 1 \end{bmatrix} \qquad \text{(Eq. 1)}$$

The system matrix is shown in Eq. 2:

$$T_{total} = T_1 \cdot T_2 \cdot T_3 \cdot T_4 \cdot T_5 = \begin{bmatrix} nx & ox & ax & px \\ ny & oy & ay & py \\ nz & oz & az & pz \\ 0 & 0 & 0 & 1 \end{bmatrix} \qquad \text{(Eq. 2)}$$

where T_1, T_2, T_3, T_4, T_5 are used to describe the transformation matrices between the joints of a robotic arm. Extract elements from the pose matrix of the end effector:

$$nx, ox, ax, px, ny, oy, ay, py, nz, oz, az, pz$$

Solving a system of nonlinear equations using the Newton's iteration method involves initializing initial guesses for joint variables, calculating function values and the Jacobian matrix based on these guesses, and applying the Newton's iteration formula to update the joint variable guesses. as shown in Eq. 3:

$$\theta_{i+1} = \theta_i - \left(\mathbf{J}^{-1}\right) \cdot f\left(\theta_i\right) \qquad \text{(Eq. 3)}$$

where θ_{i+1} is the next guess for the joint variables, θ_i is the current guess, $\mathbf{J}^{-1}$ is the inverse of the Jacobian matrix, $f\left(\theta_i\right)$ is the residuals.

The Newton iterative formula is used to solve the pose of the robotic arm as follows:

$$f_1 = ax\cos\left(\theta_2+\theta_3\right) + px\sin\left(\theta_2+\theta_3\right) + a_4\sin\left(\theta_2+\theta_3+\theta_4\right) - px \qquad \text{(Eq. 4)}$$

$$f_2 = ay\cos\left(\theta_2+\theta_3\right) + py\sin\left(\theta_2+\theta_3\right) - a_4\sin\left(\theta_2+\theta_3+\theta_4\right) - py \qquad \text{(Eq. 5)}$$

$$f_3 = nx\sin\theta_2 + ox\cos\theta_2 + px\cos\left(\theta_2+\theta_3\right) + a_4\sin\left(\theta_2+\theta_3+\theta_4\right) - px \qquad \text{(Eq. 6)}$$

$$f_4 = ny\sin\theta_2 + oy\cos\theta_2 + py\cos\left(\theta_2+\theta_3\right) - a_4\cos\left(\theta_2+\theta_3+\theta_4\right) - py \qquad \text{(Eq. 7)}$$

$$f_5 = nz\sin\left(\theta_2+\theta_3\right) + a_5\cos\left(\theta_2+\theta_3\right) \qquad \text{(Eq. 8)}$$

$$f_6 = pz - d1 - d2 - d3 - d4\sin\left(\theta_2+\theta_3+\theta_4\right) - d5 \qquad \text{(Eq. 9)}$$

The elements of the Jacobian matrix are usually calculated as the partial derivatives of the end effector position and attitude with respect to the joint variables. For the position Jacobian matrix **J** the elements of p_{ij} can be calculated as Eq. 10:

$$\mathbf{J}p_{ij} = \frac{\partial x_i}{\partial q_j}, \text{ for } i = 1,2,3 \; and \; j = 1,2,...,n \qquad \text{(Eq. 10)}$$

$\mathbf{J}p_{ij}$ describes the sensitivity of the end-effector position $x= x_1, x_2, x_3]^T$ with respect to the changes in each joint variable q_j. It calculates the variation of the end-effector position relative to the joint variables. p_{ij} represents the partial of the end-effector position in the i-th direction with respect to the j-th joint variable q_j. x_1 is the position component of the end-effector in the i-th axis direction, x_1, x_2, x_3 represent the positions of the end-effector in the x, y and z directions, respectively. q_j represents the j-th joint variable.
The final Jacobian matrix **J** is determined by the position Jacobian matrix $\mathbf{J}_p$ and attitude Jacobian matrix $\mathbf{J}_o$ composition, as shown in Eq. l1:

$$\mathbf{J} = \begin{bmatrix} \mathbf{J}_p \\ \mathbf{J}_o \end{bmatrix} \qquad \text{(Eq. 11)}$$

Like Eq 12-14 is the overall Jacobian matrix, including the mathematical formulas for the position Jacobian matrix $\mathbf{J}_p$ and the attitude Jacobian matrix $\mathbf{J}_o$:

$$\mathbf{J}_p = \begin{bmatrix} -f_1 & -a_3\sin(q_2+q_3)-a_5\sin(q_2+q_3+q_5) & -a_5\sin(q_2+q_3+q_5) & 0 & 0 \\ f_2 & a_3\cos(q_2+q_3)+a_5\cos(q_2+q_3+q_5) & a_5\cos(q_2+q_3+q_5) & 0 & 0 \\ 0 & 0 & 0 & 0 & 0 \end{bmatrix} \qquad \text{(Eq. 12)}$$

$$\mathbf{J}_o = \begin{bmatrix} 0 & 0 & 0 & 0 & 0 \\ 0 & 0 & 0 & 0 & 0 \\ 1 & 1 & 1 & 1 & 1 \end{bmatrix} \qquad \text{(Eq. 13)}$$

$$\mathbf{J} = \begin{bmatrix} -f_1 & -a_3\sin(q_2+q_3)-a_5\sin(q_2+q_3+q_5) & -a_5\sin(q_2+q_3+q_5) & 0 & 0 \\ f_2 & a_3\cos(q_2+q_3)+a_5\cos(q_2+q_3+q_5) & a_5\cos(q_2+q_3+q_5) & 0 & 0 \\ 0 & 0 & 0 & 0 & 0 \\ 0 & 0 & 0 & 0 & 0 \\ 0 & 0 & 0 & 0 & 0 \\ 1 & 1 & 1 & 1 & 1 \end{bmatrix} \qquad \text{(Eq. 14)}$$

In order to achieve accurate motion control and solve inverse dynamics problems. This paper will introduce a dynamic model construction method based on the Newton Euler iteration method, which dynamically incorporates the mass matrix, Coriolis and centrifugal forces, gravitational moments, joint velocities, and positions of the robot. By substituting the kinematic and dynamic parameters of the robotic arm, the required joint driving forces to achieve the desired motion of the end effector are derived, while also considering the external forces acting on it. This provides a solid foundation for further optimization and task-specific programming.

The dynamics of a robotic arm is an important tool for understanding its motion and forces. Here, we consider the dynamic model of a robotic arm to describe the relationship between joint acceleration $\ddot{q}$ and joint driving force τ. The dynamic equation is as Eq. 15:

$$\ddot{q} = \mathbf{M}^{-1}(q)\cdot\left(\tau - \mathbf{C}(q,\dot{q})\cdot\dot{q} - \mathbf{G}(q)\right) \quad \text{(Eq. 15)}$$

Among them, $\mathbf{M}(q)$ is the mass matrix of the robot, $\mathbf{C}(q,\dot{q})$ represents the Coriolis centrifugal force matrix, $\mathbf{G}(q)$ is the gravitational moment, $\dot{q}$ is the joint velocity, and q is the joint position.

The mass matrix describes the impact of the mass of each joint of a robot on its dynamics. It consists of the Jacobian matrix $\mathbf{J}_i$ of each joint, as well as the mass m_i and inertia matrix I_i of each joint, calculated by the following as:

$$\mathbf{M}(q) = \sum_{i=1}^{n}\left(\mathbf{J}_i^T \cdot m_i \cdot \mathbf{J}_i\right) + \sum_{i=1}^{n}\left(\mathbf{R}_i^T \cdot I_i \cdot \mathbf{R}_i\right) \quad \text{(Eq. 16)}$$

Where, n is the number of joints, $\mathbf{R}_i$ is the rotation matrix from the base to the joint i.

The Coriolis centrifugal force matrix represents the external force caused by joint angular velocity. It passes through the $\frac{\partial M_{ij}}{\partial q_k}$ and joint velocity. $\dot{q}_k$, as shown in Eq 17.

$$\mathbf{C}(q,\dot{q}) = \sum_{i=1}^{n}\left(\frac{\partial M_{ij}}{\partial q_k}\cdot\dot{q}_k\right) \quad \text{(Eq. 17)}$$

The gravitational moment describes the force acting on a robot in a gravity field. It is calculated by the joint mass m_i, the gravitational acceleration, and the joint angle $\theta_{i,j}$, and the joint position $r_{i,j}$, as shown in Eq 18.

$$\mathbf{G}(q) = \sum_{i=1}^{n}\left(m_i \cdot g \cdot r_{i,j} \cdot \cos\left(\theta_{i,j}\right)\right) \quad \text{(Eq. 18)}$$

The inverse dynamic equation is usually in the following form, where τ is the joint driving force, $\ddot{q}$ is the joint acceleration, and $\mathbf{F}$ is the external force on the end effector. By solving this equation, the joint driving force can be calculated to achieve the desired end effector action.

$$\tau = \mathbf{M}(q)\cdot\ddot{q} + \mathbf{C}(q,\dot{q}) + \mathbf{G}(q) + \mathbf{J}^T \cdot \mathbf{F} \quad \text{(Eq. 19)}$$

By substituting the kinematic and dynamic parameters from Tables 1 to 4 into Eq. 12 to 19, we can obtain the dynamic calculation model of the broiler inspection robotic arm. The maximum perimeter of the workspace of the robot can be obtained as shown in Figure 3 a,b. We conducted measurements of the aisle width and coop height in a broiler breeding house situated in Jiangsu, China. Figure 3 c-e display the workspace of the inspection robot within the coop.

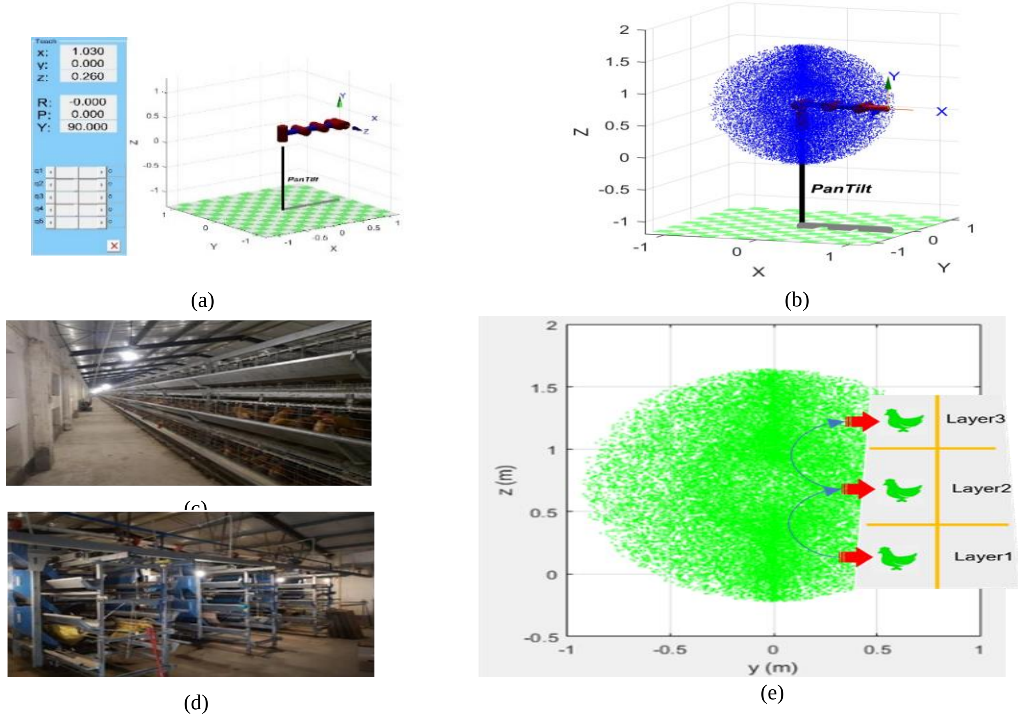

Figure 3. Robot workspace results based on Jacobian matrix.

Table 1. Links length for Pan-Tilt.

Link	Link length/mm
1	230
2	230
3	330
4	330
5	270

Table 2. All joint rotation ranges.

Joint	Range of rotation (degree)
1	-150~150
2	-100~90
3	-100~90
4	-100~100
5	-180~180

Table 3. All joint rotation ranges.

Link	Joint angle θ_i	Link offset d_i	Link length a_{i-1}	Link twist a_{i-1}
	0	d_1(0mm)	a_0(0mm)	0
2	90°	d_2=330mm	a_1(0mm)	90°
3	0	d_3(0mm)	a_2=330mm	0
4	0	d_4(0mm)	a_3=330mm	0
5	0	d_5(0mm)	a_4=270mm	0

Table 4. Dynamic parameters of the link in the simulation model.

	Mass / kg	Position of the center of mass (m)	Interia tensor / (kg * m^2)
Li	$m_1 = 18.45$ kg	${}^1p_{c_1} = (-0.081, 0.365, 0.160)$	$C_1I = \begin{bmatrix} 2508.0217 & 0.0305 & 0.0000 \\ 0.0305 & 4009.0175 & 0.0000 \\ 0.0000 & 0.0000 & 1514.2219 \end{bmatrix}$
Li	$m_1 = 26.33$ kg	${}^2p_{c_2} = (0.493, 0.486, 0.158)$	$C_2I = \begin{bmatrix} 1043.41475353 & 3.36991311 & -6.25501969 \\ 3.36991311 & 753.60814343 & -0.10070230 \\ -6.25501969 & -0.10070230 & 1252.5465276 \end{bmatrix}$
Li	$m_1 = 21.25$ kg	${}^3p_{c_3} = (0.062, 0.657, -0.078)$	$C_3I = \begin{bmatrix} 2835.4845 & 3.0998 & 78.8712 \\ 3.0998 & 2851.5548 & 103.6988 \\ 78.8712 & 103.6988 & 199.1355 \end{bmatrix}$
Li	$m_1 = 12.53$ kg	${}^4p_{c_4} = (0.056, 0.864, -0.289)$	$C_4I = \begin{bmatrix} 919.1794 & 11.6658 & 9.6213 \\ 11.6658 & 535.4080 & 408.2577 \\ 9.6213 & 408.2577 & 580.3897 \end{bmatrix}$
Li	$m_1 = 2.53$ kg	${}^5p_{c_5} = (0.066, 1.204, 0.152)$	$C_5I = \begin{bmatrix} 138.95014291 & 2.44242115 & 5.55561028 \\ 2.44242115 & 129.31168707 & 45.57594471 \\ 5.55561028 & 45.57594471 & 39.63201110 \end{bmatrix}$

Joint acceleration and uniform deceleration algorithm

The motion mode of Pan-Tilt in the inspection process is divided into linear motion of uniform acceleration-uniform velocity-uniform deceleration based (UD) on centroid offset (Zhao *et al*., 2022), and Pan-Tilt is S-curve control model, which is based on center of gravity (CG) offset and utilizes linear movement with uniform acceleration, constant velocity, and uniform deceleration, instead of curve interpolation.

The control model for this motion is represented by Eq. 20.

$$\begin{cases} a_0 = y_0, a_1 = m_0, a_2 = \dfrac{1}{h^2}\left(3\Delta_1 - m_0 h - 2m_1\right) \\ a_3 = \dfrac{1}{h^3}\left(-2\Delta + \left(m_0 + m_1\right)h\right) \\ a_4 = \dfrac{1}{h^4}\left(\Delta_1 - m_0 h\right), a_5 = \dfrac{1}{h^5}\left(\Delta_1\right) \end{cases} \quad \text{(Eq. 20)}$$

Where, a_0 represents the initial position, a_1 represents the initial velocity, a_2 is the quadratic coefficient, a_3 is the cubic coefficient used to correct the difference between acceleration and target position, a_4 is the quartic coefficient, further smoothing the interpolation curve, a_5 is the quintic coefficient, ensuring the accuracy of the final position. Compared to fifth-order interpolation, Pan-Tilt offers the advantages of simplicity and easier control. While curve interpolation can generate smoother motion trajectories, it involves higher computational complexity and consumes more system resources. The acceleration-equal-speed-equal-deceleration mode of Pan-Tilt is considered a fast motion mode. To achieve the desired target angle, the angles of link 2 and 3 are adjusted. The process involves calculating the difference between the target angle and the current angle, using acceleration to control the movement of joints 2 and 3. Subsequently, joint 1 is rotated to the target angle, allowing for the controlled motion of link 1. The control model for this process is defined by Eqs. 21-23. This method is most suitable for movements that involve sensors without the use of grasping devices. Its advantage lies in its simplicity and uniform phase. However, a notable disadvantage is the presence of step changes in acceleration. The final Pan-Tilt motion is characterized by a sigmoid curve pattern, which represents a quintic polynomial program with equal acceleration and deceleration times, but without a uniform phase. To analyze the effect of different acceleration gradients on power consumption, a comparison is made by testing various simulation movement times in the same motion mode. Finally, by examining the load and power consumption of each joint in different motion modes, the motion mode is optimized.

To calculate the acceleration time t_{acc}, the constant speed time t_{run}, and the deceleration time t_{dec}:

$$t_{acc} = \frac{v_{\max}}{a_{\max}}, t_{run} = \frac{\left\| \Theta_{t\arg 13} - \Theta_{init13} \right\|}{v_{\max}}, t_{dec} = t_{acc} \qquad \text{(Eq. 21)}$$

Where $v_{\max}$ is the maximum angular velocity, $a_{\max}$ is the maximum acceleration, init,1:3 and targ,1:3 is the initial and target joint angles, respectively.

To calculate the total time t_{total}:

$$t_{total} = t_{acc} + t_{run} + t_{dec} \qquad \text{(Eq. 22)}$$

According to the time t_{total}, calculate the joint angle theta_targ,1:3 for joints 1 to 3 in the acceleration, constant speed, followed as

$$\begin{cases} \theta_{targ,1:3(t)} = \theta_{init,13} + 0.5 a_{\max} t^2 sign\left(\theta_{t\arg,13} - \theta_{init,13}\right), \quad t < t_{acc} \\ \theta_{targ,1:3(t)} = \theta_{init,13} + v_{\max}\left(t - t_{ac}\right) sign\left(\theta_{t\arg,13} - \theta_{init,13}\right), t_{acc} \le t < t_{acc} + t_{run} \\ \theta_{targ,1:3(t)} = \theta_{t\arg,13} - 0.5 a_{\max}\left(t_{total} - t\right)^2 sign\left(\theta_{t\arg,13} - \theta_{init,13}\right), t_{acc} + t_{run} \le t \end{cases} \qquad \text{(Eq. 23)}$$

According to the design of the inspection point, it can be divided into the first layer of the initial position, the second layer, and the third layer. In order to reduce the resources required by the simulation process, the simulation environment becomes complex. The start-up process is from the initial position to the first layer position, after the first layer inspection to the second layer position, after the second layer to the third layer position, and finally to the initial position.

We implemented the rapidly-exploring random trees (RRT) planning algorithm from the *Move It* motion planning library with open motion planning library (OMPL) (Mashayekhi *et al*., 2020). The initial configuration of the robot was set to [*x*: 0.247, *y*: -0.004, *z*: 0.336], and the target position of the end-effector was defined as [*x*: 0.342, *y*: 0.0313982, *z*: 1.7579]. This allowed us to generate control signals for the kinetic model of the robot. Subsequently, we commanded the robotic arm model to move to the intended inspection location. The positions of the joints were monitored by subscribing to a ROS topic using RQT. To assess the practicality of the proposed method, we simulated a workspace within a chicken coop environment using *rviz* (Yuan *et al*., 2019), as depicted in Figure 4. The data in Table 5 were measured in the chicken coop to be used as design parameters for the robot chassis in Figure 4.

The sensor platform of the robotic arm was placed near the chicken coop, with the end-effector sensor in a state of detection across all layers. Furthermore, the robot arm needed to move to the first layer of the chicken coop for inspection, enabling the translation and tilting of the mounted sensors to capture parameters from the first layer. This approach simulated the trajectory of motion along the *z*-axis of the end-effector actuator. Subsequently, we utilized two different angle interpolation algorithms, called through ROS *via* MATLAB library files, to calculate the velocities of joint motion.

Table 5. Parameter of chassis.

Type	Value
Length of the platform	400 mm
Weight of the platform	40 kg
Height of the platform	400 mm
Width of the platform	500 mm
Wheel diameter	100 mm
Wheelbase	300 mm
Motor type Brushless	DC motor

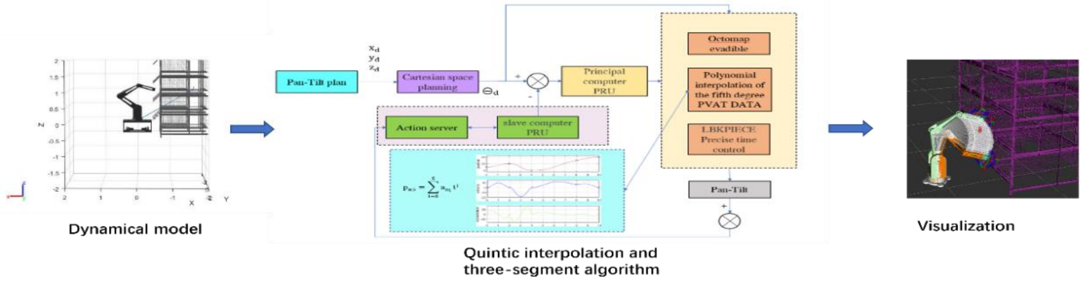

Figure 4. Principle of Pan-Tilt controller.

Analysis of the motion performance of the robot arm for inspection robot

Based on the kinematic and dynamic models described above, we calculated the speed and time of joint motion during multi-layer inspection of the robotic arm. As depicted in Figure 5, we utilized two motion modes to simulate the three layers of chicken cages in the coop of the robot. The solid line represents the S-curve motion mode, whereas the dashed line represents the uniform deceleration motion mode. During the actual inspection process, the designated position of sensor movement had the most significant impact. Only joints 2, 3, and 4 moved during this process. The peak velocities of joints 2, 3, and 4 under different exercise times, modes, and key points are presented in Figure 6. The time required for the inspection process is inversely correlated with the acceleration and deceleration time and speed of the joints.

Although the S-curve mode achieves smooth speed movement, it also increases the total inspection time. Considering the posture and running speed of the robotic arm during the inspection process, as well as the peak velocity and total running time at the same inspection points, the uniform acceleration uniform velocity uniform deceleration mode of the sensor robotic arm designed in this study is superior to the S-curve motion mode.

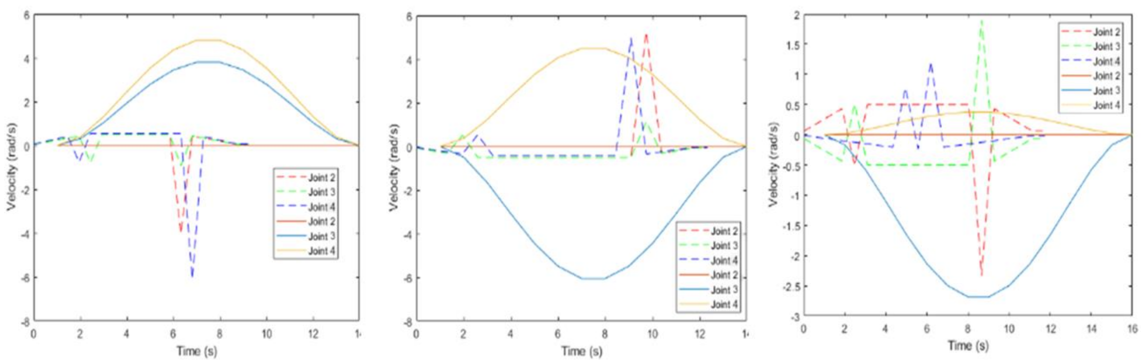

Figure 5. Fifth interpolation and acceleration constant speed deceleration robot arm speed time results.

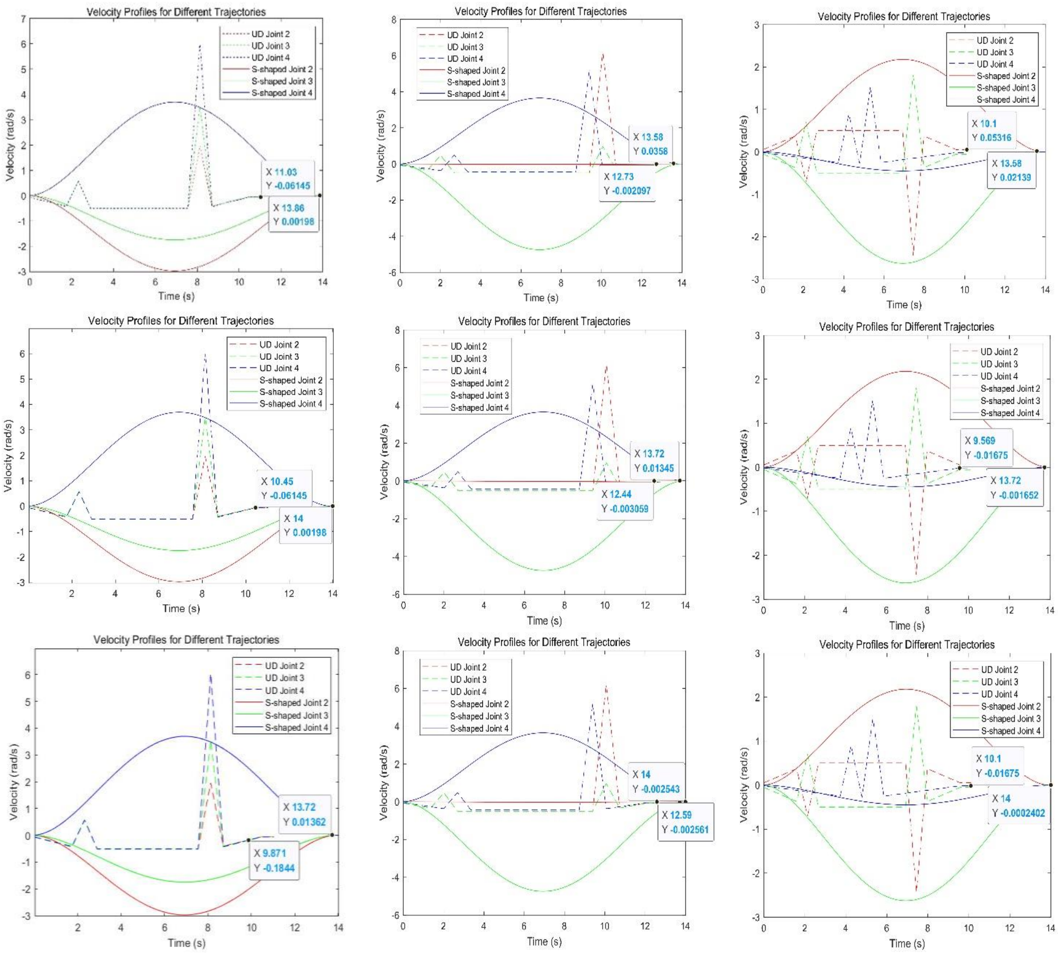

Figure 6. Velocity curve of joints 2 to 4.

Stability analysis of the inspection robot for caged broilers

Chassis structure

From the perspective of cost and system application, this article adopts a differential steering four-wheel model. The two drive wheels are controlled by two servo drivers, which adjust the speed and direction of the two wheels to achieve the forward, backward, acceleration, deceleration, and steering actions of the robot. The two driven wheels play a role in carrying and coordinating steering. Figure 4 shows the motion model of a differential steering four-wheel vehicle.

$$\Delta X = \frac{r}{2}\frac{v_l + v_r}{v_l - v_r}\sin\Delta\theta \qquad \text{(Eq. 24)}$$

$$\Delta Y = \frac{r}{2}\frac{v_l + v_r}{v_l - v_r}\left(1 - \cos\Delta\theta\right) \qquad \text{(Eq. 25)}$$

$$d\Delta\theta = \frac{v_l + v_r}{2}\Delta t \quad \text{(Eq. 26)}$$

$$\Delta X = d\sin\Delta t \quad \text{(Eq. 27)}$$

Eqs. 24-27 constitute the motion model of a differential-drive robot, providing a mathematical framework for analyzing its kinematic behavior. To enhance the accuracy of displacement estimation during steering, Eq. 24 extends the computation of ΔX by explicitly accounting for the differential velocities between the two wheels, enabling a more precise description of the robot's trajectory under turning conditions. Eq. 25 models the lateral displacement ΔY along the Y-axis induced by rotational motion, capturing the lateral deviation inherent to the robot's curved trajectory. Eq. 26 defines the change in the robot's yaw angle, $d\Delta\theta$,by integrating the average linear velocities of the left and right wheels (v_l and v_r) over a given time increment Δt This calculation establishes the robot's angular displacement as a function of wheel velocities. Eq. 27 computes the linear displacement ΔX along the X-axis, which is influenced by the angular change ($\Delta\theta$) and the effective turning radius *r*. Together, these equations form a comprehensive model for predicting motion trajectories and displacement variations, providing a robust foundation for trajectory tracking and motion planning in differential-drive robots.

As shown in Figure 7, this model is established to calculate the shift of the motion state of the robot when it turns on the turf (surface). Eqs. 26 and 27 are derived from Eqs. 24 and 25, and the running speed of the left wheel of the robot is v_l and the running speed of the right wheel is v_r, *r* is the turning radius of the robot, used to more accurately describe the displacement in the *X* direction under different speed ratio conditions.

The robot moves in a circular arc along point A with a turning radius of *d*. It can be concluded that the deviation angle of robot motion is $\Delta\theta$. The deviation arc of robot motion can be obtained from the relation formula of the left and right wheel speed $\Delta\theta$: when the robot moves in a circular motion, the shift on the *X* axis is ΔX , the change on the *Y* axis is Δy. The relationship between *Y* and turning arc $d\Delta x$ can be obtained. Δ realizes the relationship between *Y* and the running speed of the left and right wheels by changing v_r and v_l and realizes motion control such as vehicle correction and steering.

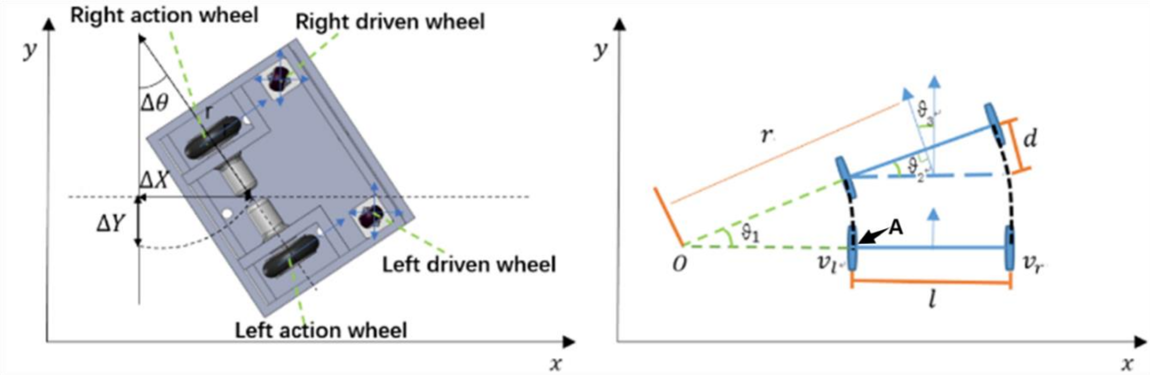

Figure 7. Chassis kinematic model.

Analysis of turning stability of robotic arm on chassis

According to the load position above the centerline of the body, we can assume that the load is uniformly distributed above the body, that is, the load center is located above the centerline of the body and the height h above the ground. Therefore, the height of the CG of the mobile platform can be approximated by the height h above the centerline of the body plus half of the height of the body, through experiments and measurements, we determined that the total height of the body is 400 millimeters. Therefore, the CG height can be specifically calculated as h+200 mm. The distance between the wheel(support points) is L, and the distance between the wheel(support points) on the right line and the centerline of the body is x, the horizontal distance from the centerline to the support point is $\frac{L}{2}-x$, the distance between the CG and the right wheel is $d_{cg-support}$ followed as Eq. 28.

$$d_{cg-support} = \sqrt{h^2 + \left(\frac{L}{2} - x\right)^2} \quad \text{(Eq. 28)}$$

Among them, the tilt angle can be calculated from the roll angle, which is equal to the tangent value of the roll Angle multiplied by 180 degrees /π. The weight m is equal to the body weight m_b plus the load weight m_o, F_C represents the Rollover force when the CG shifts, h_m is the height at which the deflection occurred. α is the moving angle. For the given parameters and Eqs. 28-30, we can do the calculation (Eq. 31):

$$m = m_b + m_o \quad \text{(Eq. 29)}$$

$$F_C = \frac{m \times d_{cg-support}}{h_m \times \sin\alpha} \quad \text{(Eq. 30)}$$

$$h = \frac{h_b}{2} + z_o \quad \text{(Eq. 31)}$$

where z_0 represents the additional CG height. Rollover force as calculation:

$$F = \frac{m \cdot \sqrt{h^2 + \left(\frac{L}{2} - x\right)^2}}{\sqrt{h^2 + \left(\frac{L}{2}\right)^2} \cdot \sin\left(\arctan\left(\frac{x}{h + \frac{L}{2}}\right) \cdot \frac{180}{\pi}\right)} \qquad \text{(Eq. 32)}$$

In the paper, we evaluated the impact of CG offset at different heights on pressure distribution supported by two primary driving wheels. During the transition from the initial position to the first layer, the center of CG of the gimbal mechanism shifts by 75 millimeters. The offset increases to 150 millimeters between the first and second layers, followed by an additional shift of 83 millimeters from the second to the third layer. Considering the total mass of the gimbal mechanism as 25 kilograms, combined with approximately 30 kg of driving equipment, the overall system mass reaches 55 kilograms. The maximum center of CG offset observed is 150 millimeters. Utilizing the relationship between pressure and CG offset, and based on Eq. 32, the maximum pressure is calculated to be 300 Newtons (where g=9.8 m/s^2) represents gravitational acceleration). This pressure value is significantly lower than the maximum pressure of 476.04 Newtons, which occurs at a displacement of 225.92 millimeters under edge instability conditions with a tilt angle tangent of 15.90 degrees. These findings indicate that even under the most extreme center of CG shift scenarios, the pressure remains within a safe operational range, thus ensuring the structural integrity of the equipment and minimizing the risk of mechanical failure.

Results and Discussions

Center of gravity deflection test of the Pan-tilt on the chassis

In the paper, we analyzed the motion trajectory of the robot performing inspection tasks in a chicken coop to assess the impact of different motion patterns on joint speed and total movement time. Considering the practical application of the robot, four key positions were defined: starting position T_1= (0.0, 0.023, 1.398), first layer T_2= (0.393, 0, -0.525), second layer T_3= (0.466, -0.005, 0.239), and third layer T_4= (0.393, 0.000, 0.470). These position points describe the motion trajectory of the robot as it moves from the initial position to the different levels of the chicken cages. To compare the performance of the Uniform Acceleration-Uniform Velocity-Uniform Deceleration (UD) mode with the S-curve mode in actual inspection operations, we analyzed the joint velocities and total movement times for each mode, as shown in Figure 8. The results indicated that the minimum time from the three segments of motion was used as a reference for time calculations.

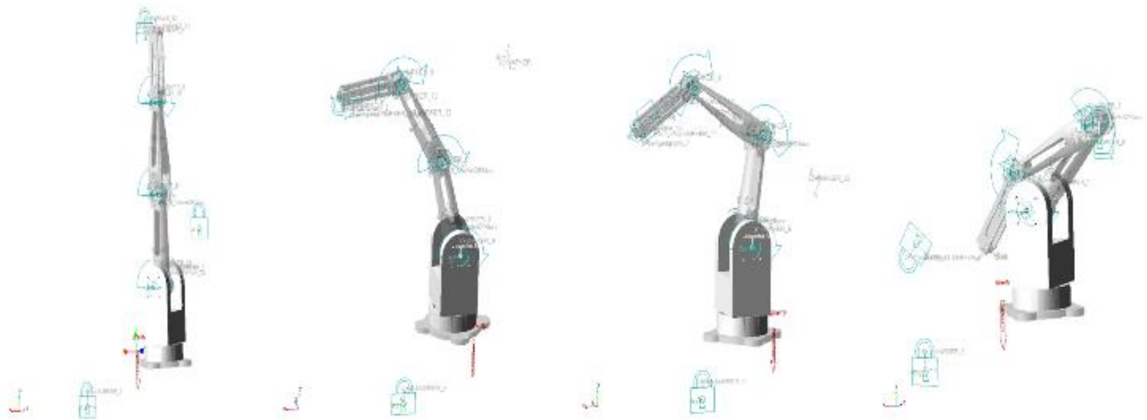

Figure 8. Robot center of gravity deflection experiment.

In the UD mode, the acceleration and deceleration times for the joints increased with the height of the movement levels. For example, the acceleration and deceleration times for Joint 2 at the first, second, and third layers were 2.5s, 3.1s, and 4.3s, respectively. The total movement times were 9.8s, 12.44s, and 9.5s for the corresponding layers. These data suggest that the total movement time is directly related to the acceleration and deceleration times, typically indicating that longer acceleration and deceleration times result in longer total movement times.

In contrast, the S-curve mode exhibited smooth velocity transitions during the acceleration and deceleration phases, with acceleration and deceleration times for Joint 2 recorded as 13.72 seconds, 12.59 seconds, and 10.1 seconds, respectively. These times were generally higher than those observed in the uniform acceleration mode, reflecting the smooth transition characteristics of the S-curve mode. Although the S-curve mode provides a smoother change in velocity, the total movement times were also increased, recorded as 13.72 seconds, 12.59 seconds, and 10.1 seconds for the respective layers. Overall analysis indicates that while the S-curve mode offers smoother velocity changes, its longer acceleration and deceleration times result in increased total movement times. Therefore, to ensure the robot maintains a stable posture and enhances operational efficiency during inspections, the UD mode proves to be superior in optimizing peak joint velocities and total movement times. This mode not only improves motion efficiency but also effectively reduces total movement times, making it more suitable for inspection tasks in practical applications.

Test results and analysis for detecting energy consumption of manipulator joints

In order to comprehensively understand the behavior of the robot under different structural configurations, experiments were conducted at layer heights of 30, 45 and 60 cm, taking factors such as the intermediate partition into account. The conditions labeled “A”, “B”, and “C” correspond to experiments simulating the power consumption of the robot joints at different cage heights. Select the power consumption of the sensor pan tilt as the third evaluation indicator, as the main power consumption of the inspection robot comes from the movement of the sensor pan tilt between the cage layers, rather than the mobile chassis. Patrol is an unstructured repetitive operation. The introduction of joint power consumption can more comprehensively demonstrate the advantages and disadvantages of harvesting robots, as well as the direction for further optimization. According to Figure 9 a-c, the power consumption of the pan tilt frame is mainly in joint two, while the power consumption of joints three and four is mainly in different qualities of the sensors. This is because the number and type of sensors carried by joint five are different, while joint five does not move during inspection. As shown in Figure 9d, the shift in the position of the inspection cage layer will alter the movement of joint two during the rise and fall process, OptimizeG refers to the optimized energy consumption algorithm for the robotic arm. However, compared to Joint 2, the power consumption of Joint 3 and Joint 4 is less affected by the position of the cage layer. More than 80% of the power of the Joint 2 inspection robot arm is consumed the most. The highest power consumption of Joint 2 is mainly due to the fact that in the three stages of the first, second, and third layers, Joint 2 must overcome the gravity of Joint 3, 4, and 5. Due to the tiny load of connector five, its total power consumption is the smallest among connectors 1-5. The power consumption of joints three and four in the uniform deceleration motion mode is lower than that in the S-curve motion mode, and the power consumption of both joints decreases with the extension of the working cycle.

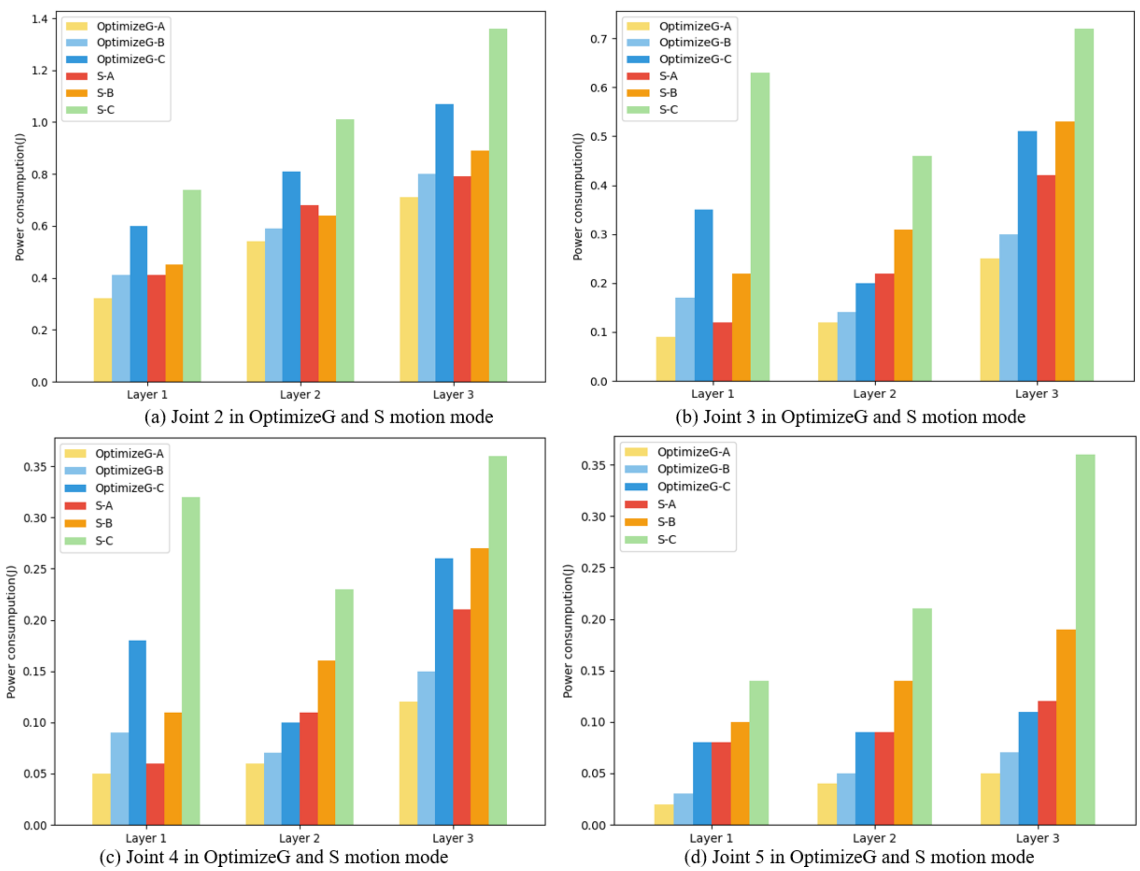

Figure 9. Comparing the power consumption of chicken coop inspection between quintic interpolation and accelerated uniform deceleration algorithms.

Using the S-curve motion mode, except for G-A and S-A, the power consumption of connector two is uniformly higher than that of the uniformly accelerated and decelerated motion mode in the test. In terms of the total power consumption of the sensor head, the uniform speed uniform deceleration motion mode is superior to the s-curve motion mode. Compared to using the S-curve motion mode, the power consumption of the sensor head in the uniform acceleration, uniform speed, and uniform deceleration motion mode is reduced by 0.056J in G-B, which is the minimum power consumption reduction. In G-C, the reduction is 1.902J, which is the maximum power consumption reduction. In summary, from the perspective of reducing the total consumption of sensor heads, the uniform speed uniform deceleration motion mode is superior to the S-curve motion mode. Among all joints of the sensor head, joint two has the highest power consumption, which needs to be optimized in future research. The position of the sub entity frame is designed more properly, which can cancel the movement of connector two during the sub entity and reset process, further saving power consumption. Alternatively, optimize the inspection methods and algorithms. Previously, numerous inspection robots mainly focused on the workspace and motion performance of the chassis and robotic arm, or the planning of motion paths. In this study, not only the motion performance of the chassis and sensors was analyzed and anti-roll analysis was conducted, but also the inspection power during pan tilt was analyzed. Although this study was conducted in an environment with only gravity, its power analysis method points the way for the next step of optimizing the structure and motion control of sensor heads.

Conclusions

During the experimental process, we evaluated the performance of the designed and simulated robot. The results showed that the ground motion chassis and sensor gimbal structure of the robot met the design requirements and were suitable for cage-reared chicken inspections.

Furthermore, the established kinematic models for the ground motion chassis and sensor gimbal structure provided a solid foundation for additional research and development of the control system of the robot. These models can be used to optimize the movement of the robot and improve its inspection capabilities. By analyzing and optimizing the center of gravity of the sensor gimbal during movement between different cage layers, we were able to minimize the maximum center of gravity offset on the ground plane. This optimization significantly improved the stability of the robot during inspection, ensuring reliable operation and accurate data collection.

Moreover, we compared the performance of the weight-priority uniform acceleration-uniform velocity-uniform deceleration movement mode and the S-curve movement mode for the sensor gimbal. The results showed that the weight-priority uniform acceleration-uniform velocity-UD movement mode had a shorter maximum conversion time between cage layers, thus improving inspection efficiency. In summary, the designed and simulated the ground motion chassis and sensor gimbal structure of the robot met the design requirements for cage-reared chicken inspections. The established kinematic models provided a solid foundation for additional research and development of the control system. Optimizing the center of gravity of the sensor gimbal enhanced stability during inspections, while the weight-priority movement mode-featuring uniform acceleration, uniform velocity, and uniform deceleration-greatly increased inspection efficiency. These findings contribute to the development of automated systems for the inspection of cage-reared chickens, promoting the modernization and sustainability of the animal industry.

Acknowledgments: the project was supported by National Key R&D Program of China (2023YFD2000800), supported by Open Fund of Key Laboratory of Smart Breeding (Co-construction by Ministry and Province), Ministry of Agriculture and Rural Affairs(2023-TJAULSBF-2401), supported by China Agriculture Research System of MOF and MARA" (CARS-41), supported by National Key R&D Program of China (2022YFD1601900), supported by Research on Precise Ventilation Mode for Poultry Broiler Cage Rearing in a Multi-Layer System.

References

Xie D., Chen L., Liu L., Chen L., and Wang H. 2022, Actuators and Sensors for Application in Agricultural Robots: A Review. Machines 10(10): 913.

Nguyen V. L., Lin C.-Y., Kuo C.-H. 2020. Gravity Compensation Design of Planar Articulated Robotic Arms Using the Gear-Spring Modules. Journal of Mechanisms and Robotics-Transactions of the Asme 12(3): 031014.

Xiao L., Ding K., Gao Y., and Rao X. 2019. Behavior-induced health condition monitoring of caged chickens using binocular vision. Computers and Electronics in Agriculture 156: 254-262.

Rea P., Ottaviano E. 2018. Design and development of an Inspection Robotic System for indoor applications. Robotics and Computer-Integrated Manufacturing. 49: 143-151.

Ren G., Lin T., Ying Y., Chowdhary G., Ting K. C. 2020. Agricultural robotics research applicable to poultry production: A review. Computers and Electronics in Agriculture. 169: 105216.

Sun Y., Guan L., Chang Z., Li C., Gao Y. 2019. Design of a Low-Cost Indoor Navigation System for Food Delivery Robot Based on Multi-Sensor Information Fusion. Sensors. 19(22): 4980.

Tzitzis A., Megalou S., Siachalou S., Yioultsis T., et al. 2019. Phase ReLock - Localization of RFID Tags by a Moving Robot. in 13th European Conference on Antennas and Propagation (EuCAP), Krakow, POLAND.

Cheng M., Xiang D. 2020. The Design and Application of a Track-type Autonomous Inspection Robot for Electrical Distribution Room. Robotica, 38(2): 185-206.

Karpyshev P., Ilin V., Kalinov I., Petrovsky A., Tsetserukou D. 2021. Autonomous Mobile Robot for Apple Plant Disease Detection based on CNN and Multi-Spectral Vision System. in IEEE/SICE International Symposium on System Integration (SII), Electr Network. 2021: 157-162.

Cai J., Deng J., Zhang W., Zhao W. 2021. Modeling Method of Autonomous Robot Manipulator Based on D-H Algorithm. Mobile Information Systems. 2021: 4448648.

Razak A., Abdullah K., Kamarudin K., Saad F.S.A., Shukor S. A., Mustafa H., Bakar M. A. A. 2016. Mobile robot structure design, modeling and simulation for confined space application. in 2016 2nd IEEE International Symposium on Robotics and Manufacturing Automation (ROMA). 2016: 1-5.

Yang H., Chen L., Ma Z. B., Chen M., Zhang Y., Deng F., Li M. 2021. Computer vision-based high-quality tea automatic plucking robot using Delta parallel manipulator. Computers and Electronics in Agriculture. 181: 105946.

Quaglia G., Visconte C., Scimmi L. S., Melchiorre M., Cavallone P., Pastorelli S. 2019. Robot arm and control architecture integration on a UGV for precision agriculture. in Advances in Mechanism and Machine Science (Mechanisms and Machine Science, 2019: 2339-2348.

Paradkar V., Raheman H., K R., Development of a metering mechanism with serial robotic arm for handling paper pot seedlings in a vegetable transplanter. Artificial Intelligence in Agriculture. 5: 52-63.

Raikwar S., Fehrmann J., Herlitzius T. 2022. Navigation and control development for a four-wheel-steered mobile orchard robot using model-based design. Computers and Electronics in Agriculture. 202: 107410.

Zhao J., Wu C. C., Yang G. L., Chen C. Y., Chen S., Xiang C. Y., Zhang C. 2022. Kinematics analysis and workspace optimization for a 4-DOF 3T1R parallel manipulator. Mechanism and Machine Theory. 167: 104484.

Yoo J., Huh H. 2020. Optimization of Three-Wheel Vehicle Roof Structures Against Rollover Accidents. International Journal of Automotive Technology. 21: 795-804.

Xue H., Li L., Wen P., Zhang M. 2023. A machine learning-based positioning method for poultry in cage environments. Computers and Electronics in Agriculture. 208:107764.

Mishra G., Ahluwalia U., Praharaj K., Prasad S. 2019. RF and RFID based Object Identification and Navigation system for the Visually Impaired. in 32nd International Conference on VLSI Design (VLSID) / 18th International Conference on Embedded Systems (ES), New Delhi. 2019: 533-534.

Xu Q., Li H., Wang Q., Wang C. 2021. Wheel Deflection Control of Agricultural Vehicles with Four-Wheel Independent Omnidirectional Steering. Actuators, 10(12): 334.

Saeedi B., Sadedel M. 2021. Implementation of Behavior-Based Navigation Algorithm on Four-Wheel Steering Mobile Robot. Journal of Computational Applied Mechanics. 52(4): 619-641.

Zhang Y., Zhang M., Li M. 2022. Agricultural Internet of Things. in Sensing, Data Managing, and Control Technologies for Agricultural Systems. 2022:17-40.

Zhang D., Han X. 2020. Kinematic Reliability Analysis of Robotic Manipulator. Journal of Mechanical Design. 142(4): 044502.

Catanoso D., Chakrabarty A., Fugate J., Naal U., Welsh T. M., Edwards L. J., OceanWATERS Lander Robotic Arm Operation. in IEEE Aerospace Conference (AeroConf), Electr Network, 2021: 2021.

Chen J., Qiang H., Wu J., Xu G., Wang Z. 2021. Navigation path extraction for greenhouse cucumber-picking robots using the prediction-point Hough transform. Computers and Electronics in Agriculture, 180:105911.

Almasri E., Uyguroglu M. K. 2021. Modeling and Trajectory Planning Optimization for the Symmetrical Multiwheeled Omnidirectional Mobile Robot. Symmetry-Basel. 13(6): 1033.

Liu Z., Lv Z., Zheng W., Wang X. 2022. Trajectory Control of Two-Degree-of-Freedom Sweet Potato Transplanting Robot Arm. Ieee Access, 10: 26294-26306.

Le A. V., Hayat A. A., Elara M. R., Nhan N. H. K., Prathap K. 2019. Reconfigurable pavement sweeping robot and pedestrian cohabitant framework by vision techniques. IEEE Access. 7: 159402-159414.

Mashayekhi R., Idris M. Y. I., Anisi M. H., Ahmedy I., Ali I. 2020. Informed RRT*-connect: An asymptotically optimal single-query path planning method. IEEE Access, , 8: 19842-19852.

Yuan C., Zhang W., Liu G., Liu G. F., Pan X. L., Liu X. H. 2019. A heuristic rapidly-exploring random trees method for manipulator motion planning. IEEE access. 8: 900-910.